



Full Length Article

Quantitative analysis of multiple deformation mechanisms in NiCrCoFe high-entropy alloy

Jun Chen ^a, Zhaoyang Hou ^{a,*}, Zhen Wang ^{a,*}, Kefan Li ^a, Pengfei Zou ^a, Kejun Dong ^b, Gang Shi ^a^a School of Science, Chang'an University, Xi'an, Shaanxi 710064, China^b School of Engineering, Design and Built Environment, Western Sydney University, Penrith, NSW 2751, Australia

ARTICLE INFO

Keywords:

High entropy alloys
Deformation mechanism
Martensitic transformation
Grain size
Molecular dynamic simulation

ABSTRACT

Multiple deformation mechanisms were often observed during the deformation processes of high-entropy alloys (HEAs), but the quantitative analysis of the contribution of different deformation mechanisms to the total deformation is few involved. In this work, the multiple deformation mechanisms in NiCoCrFe HEA are studied by molecular dynamics (MD) method. The average flow stress transforms from Hall-Petch (HP) relationship to inverse Hall-Petch (IHP) relationship with grain refinement at critical grain size ($d_c \approx 27.31$ nm). And the microstructural evolutions of microstructures during the deformation process are revealed by means of the crystal-analysis-tool (CAT). The contributions of various microstructural configurations to the total deformation are systematically studied by means of post-processing metrics. In the strengthening regime, the deformation mechanisms are dominated by stacking fault, grain boundary (GB) activity, and HCP martensitic transformation, accompanied with twinning and dislocation. In the softening regime, the deformation mechanisms are dominated by GB activity and stacking fault. The deformation mechanisms revealed according to the percentages of total strain accommodated by various microstructural configurations is more accurate than their atomic fractions. These results would provide an accurate and deep insight into the multiple deformation mechanisms of HEAs.

1. Introduction

Multi-component alloys, often referred to as high-entropy alloys (HEAs), were initially reported by Yeh [1] and Cantor [2]. Unlike conventional alloys with one or rarely two base elements, HEAs contain multi-principal elements with equiatomic or near equiatomic concentrations. Due to the high configurational mixing entropy of HEAs, it prefers to form a single-phase solid solution with body-centered cubic (BCC), face-centered cubic (FCC), or close-packed hexagonal (HCP) structure [3]. Owing to the unique microstructure, HEAs usually exhibit many excellent mechanical properties, such as ultrahigh hardness, high tensile strength, good ductility, high thermal softening resistance, remarkable irradiation resistance, and good wear resistance [4–7]. It is thought to be a promising structure material and has recently attracted enormous attention over worldwide in the fields of solid mechanics and material sciences [8].

The mechanical properties and deformation mechanisms of most metals and alloys are strongly influenced by their grain size. As the grain size reduces from microscale to nanoscale, the yield stress, flow stress

and hardness usually increase with reducing grain size [9–11]. This relationship, known as Hall-Petch (HP) relationship [12,13] and has been well established experimentally in the past half century [14]. However, this strengthening is broken below a critical grain size d_c , typically in the range of 10–30 nm, and then decreases with the further reduction of grain size, exhibiting an inverse Hall-Petch (IHP) relationship [15–17]. Many experimental and simulation studies [14–21] have observed that the HP strengthening comes from the effective obstruction of grain boundaries (GBs) to dislocation slip, while the IHP softening is attributed to the GB activities, such as sliding and rotation. As with pure metals and conventional alloys, the HP strengthening and IHP softening were also reported in HEAs [22–29]. However, beside the dislocation and GB activity, multiple deformation mechanisms of stacking fault, twinning, and FCC → HCP martensitic transformation were often observed in HEAs due to their relatively low stacking fault energy [30–38]. The experimental observations in CoCrFeMnNi HEA by Otto et al. [30] showed that when the temperature is decreased from 293 K to 77 K, the deformation mechanism changes from dislocation slide dominated plasticity to a mixed deformation mode consisting of

* Corresponding authors.

E-mail addresses: zhaoyanghou@163.com (Z. Hou), wangzhen@chd.edu.cn (Z. Wang).

dislocation slide plus nanoscale twinning. Real-time observations in dual-phase CrMnFeCoNi HEA by Chen et al. [31] displayed that the stacking fault networks formed in the deformation process serve as barriers to dislocation gliding on intersecting planes and provide the dominant contribution to strain hardening. Recently, Wei et al [32,33] found that the stacking fault energy of CoCrFeMnNi HEA can be reduced by composition modification or Mo minor addition, and the plastic deformation mechanism varies from the predominant dislocation slip accompanied with twinning to the FCC → HCP martensitic transformation. In previous experimental studies [30–38], the underlying deformation mechanism in HEAs is inferred from indirect quantitative measurements, such as work hardening rate, SF probability, texture intensity or appearance of defect configurations as a function of applied loading. However, the relative contributions of individual mechanisms (e.g. dislocation, GB activity, twinning, stacking fault, martensitic transformation, etc.) to total deformation and their competitions with grain refinement are few investigated.

Molecular dynamics (MD) simulations provide an atomic-scale insight into the deformation mechanism of materials, and tremendous advances in understanding the mechanical behavior and plastic deformation of HEAs have been achieved [22,24,37–40]. These studies tracked the evolution of various defect configurations (e.g. GB, dislocation, twinned boundary, stacking fault, etc) participating in a given deformation mechanism, and the dominant deformation mechanism is identified according to their atomic fraction. However, these studies provide only a qualitative picture of deformation mechanisms, since the contribution of different atoms to the total deformation may be different. And it has been suggested the contribution of individual deformation mechanism to the overall deformation is best quantified by the amount of total strain it accommodates [41]. Recently, Tucker and coworkers [42–45] developed a set of post-processing metrics, based on continuum mechanics, to calculate the contribution of various mechanisms to the overall deformation by resolving the associated fraction of total strain accommodation to individual operative mechanisms, and the usefulness of this method has been presented in identifying the key deformation mechanism in nanocrystalline metals.

Among the single-phase FCC structured HEAs, NiCoCrFe-based HEAs are intensively studied because of their unique combination of outstanding fracture toughness, exceptional ductility, and superior fatigue resistance especially at cryogenic temperature [30–32,46,47]. Beside the dislocation slip, multiple deformation mechanisms of twinning, stacking fault, and FCC → HCP martensitic transformation often appear during their deformation processes [32–39,48]. In this work, the tensile process of NiCoCrFe HEA with different grain sizes is simulated by MD method. A quantitative analysis of the contribution of various deformation mechanisms to the total deformation, including GB activity, dislocation, twinning, stacking fault, and FCC → HCP martensitic transformation, is systematically studied by means of the post-processing metrics proposed by Tucker and coworkers [42–45]. The grain-size dependent mechanical behavior and the competition of various deformation mechanisms with grain refinement are revealed. These results would provide an accurate and deep insight into the multiple deformation mechanisms of HEAs and offer some clues for the engineering strategy to design high performance HEAs at small-scales.

2. Computational methods

2.1. Molecular dynamics simulation

MD calculations are performed using the Large-Scale Atomic/Molecular Massively Parallel Simulator (LAMMPS) [49]. The interaction between atoms in NiCoCrFe system is described by the second nearest-neighbor modified embedded-atom method (2NN MEAM) proposed by Choi et al. [50]. This potential function has been widely used to study the deformation mechanism and mechanical properties of NiCoCrFe HEA in previous studies [51–55], and it has been found that this

potential function can accurately reflect the basic structural and physical characteristics of NiCoCrFe HEA, including lattice constant, cohesive energy, and elastic modulus.

Initial polycrystalline structure with single FCC phase is constructed by Voronoi tessellation scheme, containing six grains with random crystallographic orientations, as shown in Fig. 1. The lattice constant is chosen to be 3.54 Å according to previous simulations and experiments [56,57]. Ni, Co, Cr, and Fe atoms are completely random distribution and reach equal molar composition (Ni: Co: Cr: Fe = 1: 1: 1: 1) to generate an equiatomic NiCoCrFe HEA with single-phase FCC structure. To illuminate the effect of grain size, seven polycrystalline structures with average grain size reducing from 47.80 nm to 6.83 nm are constructed by adjusting the size of simulating box. Correspondingly, they contain 30927559 ~ 90169 atoms, as shown in Table 1. The number of grains and crystallographic grain orientation remain constant when adjusting the grain size.

At the beginning of simulation, each initial configuration is isothermally relaxed for 100 ps at 300 K and then performed a Monte Carlo (MC) simulation for 10,000 MC steps to obtain equilibrium atomic configuration. Periodic boundary conditions are applied to all directions. As shown in Fig. 1(b), Ni, Co, Cr, and Fe atoms are uniformly distributed in the simulating box. Subsequently, the seven polycrystalline samples are uniaxial tensioned at a strain rate of $1.0 \times 10^9 \text{ s}^{-1}$ along the x direction at 300 K under isothermal-isobaric ensemble (NPT) ensemble.

2.2. Identification of microstructural configurations

In the simulation of tensile process, the atom types with FCC, HCP, BCC, and disordered local structures are characterized by common neighborhood analysis (CNA) [58]. In this work, the FCC and HCP atoms gather into grains, while the disordered atoms usually locate at the GBs and dislocation cores. Different assembling of HCP atom layers will form various planar defects, such as intrinsic stacking fault, extrinsic stacking fault, twin boundary and martensite structure, as shown in Fig. 2. Two adjacent HCP atom layers are identified as an intrinsic stacking fault, which usually is behind the $1/6 \langle 112 \rangle$ Shockley partial dislocation. Two layers of HCP atoms with one FCC atom layer between them stands for an extrinsic stacking fault, while two layers of HCP atoms with more than one FCC atom layer between them is referred as a twin boundary. More than three adjacent HCP atom layers is identified as a martensite structure. These planar defects usually play a crucial role in the plastic deformation mechanism of HEAs, and they are identified by means of the crystal-analysis-tool (CAT) proposed by Stukowski [59]. In the following section, atoms with configurations of intrinsic stacking fault, extrinsic stacking fault, twin boundary, and martensite structure are colored in blue, yellow, pink, and red, respectively. The dislocations appearing in the deformation process are identified by means of the dislocation analysis (DXA) module in OVITO [60].

2.3. Quantification of various deformation mechanisms

The role of individual deformation mechanism is resolved as a percentage of total strain accommodated in the loading direction at any point during uniaxial loading, using the continuum-based kinematic metrics proposed by Tucker and coworkers [42–45]. For this purpose, the strain tensor of each atom is first calculated from the atomic deformation gradient tensor by mapping the changes in the atomic positions of the nearest neighbors after deformation. The deformation gradient tensor (\mathbf{F}^α) of atom α is defined as

$$\mathbf{F}^\alpha = \left(\sum_{\beta=1}^N (\mathbf{x}^{\alpha\beta})(\mathbf{X}^{\alpha\beta}) \right) \left(\sum_{\beta=1}^N (\mathbf{X}^{\alpha\beta})(\mathbf{X}^{\alpha\beta}) \right)^{-1} \quad (1)$$

Here, β is the neighbor of atom α , N is the neighbor number of atom α . $\mathbf{x}^{\alpha\beta}$ and $\mathbf{X}^{\alpha\beta}$ are the slip vectors between atom α and atom β in the

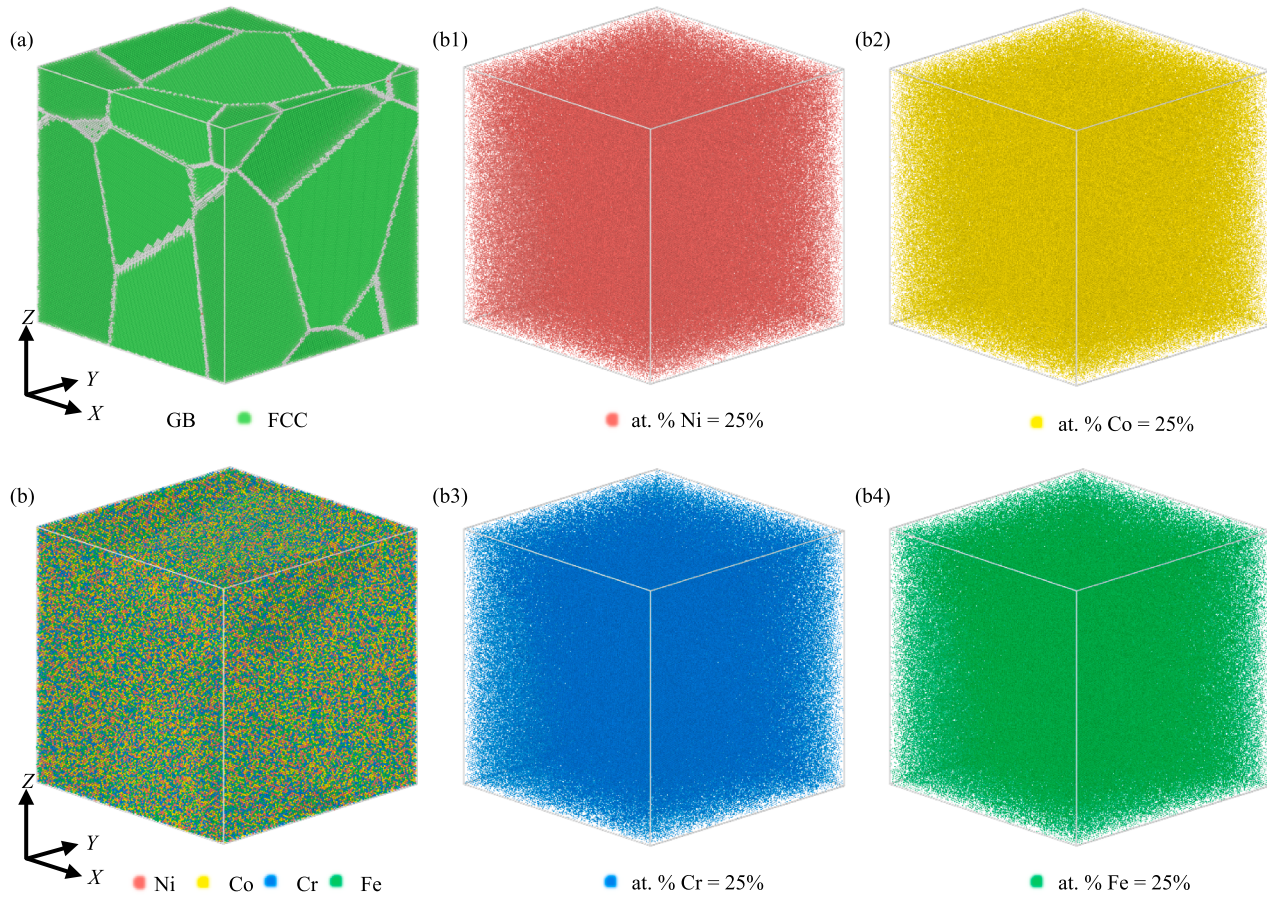


Fig. 1. Initial microstructural configuration of NiCoCrFe high-entropy alloy. (a) Polycrystalline structure with six grains and FCC lattice. (b) Distributions of Ni, Co, Cr, and Fe atoms.

Table 1
Model parameters of NiCoCrFe high-entropy alloy with different grain sizes.

Average grain size (nm)	Number of grains	Dimensions (nm ³)	Total number of atoms
47.80	6	70 × 70 × 70	30,927,559
40.97	6	60 × 60 × 60	19,476,186
34.14	6	50 × 50 × 50	11,270,980
27.31	6	40 × 40 × 40	5,770,598
20.48	6	30 × 30 × 30	2,434,438
13.65	6	20 × 20 × 20	721,293
6.83	6	10 × 10 × 10	90,169

deformed and reference configurations, respectively. The strain tensor (E^{α}) of atom α is calculated as

$$E^{\alpha} = \frac{1}{2} [(\mathbf{F}^{\alpha})^T \mathbf{F}^{\alpha} - \mathbf{I}] \quad (2)$$

where \mathbf{I} is the identity tensor.

To calculate the total strain accommodated by individual deformation mechanisms, all atoms are classified into different groups corresponding to a given mechanism (i.e., GB activity, dislocation, stacking fault, twinning, and martensite transformation). As shown in Fig. 3, the disordered atoms in GBs and dislocation cores both have high shear strain, but they are classified into different groups of GB activity and dislocation, respectively, as their different dynamic behaviors. The planar defects of intrinsic stacking faults, extrinsic stacking faults, twin boundaries, and martensite structures all have high shear strain. The stacking fault group contains the intrinsic stacking fault and extrinsic

stacking fault. The twinning group includes the twin boundary with one-layer HCP atoms and their coordinated FCC atoms being traversed by the migration of twin boundary. The martensite transformation group includes the HCP atoms with martensite structure. Remaining FCC atoms that do not belong to either the stacking fault group or twinning group, deformed in an elastic manner, and are classified into the grain-elastic group.

The percentage of total loading strain p_k , accommodated by a deformation mechanism k , is given by

$$p_k = \frac{\sum_{i=1}^{n_k} E_{xx}^i}{\sum_{i=1}^{NN} E_{xx}^i} \quad (3)$$

Here, E_{xx}^i is the normal component of the strain tensor of atom i along the loading direction (x in this case), n_k is the number of atoms participating in the deformation mechanism k , while NN is the total number of atoms in the system.

3. Results and discussions

3.1. Grain-size dependence of mechanism behavior

Fig. 4 shows that the stress-strain curves of NiCoCrFe HEA with various grain sizes (d) during the uniaxial tension. It can be found that the stress-strain curves show linear relationship in the initial elastic stage (ϵ : 0–4 %), and the elastic moduli decreases with the reduction of grain size. This is mainly due to the increase of disordered GB atoms with decreasing grain size, which will cause lower elastic stiffness. The simulation result of elastic moduli with grain size of 47.80 nm is 166.1

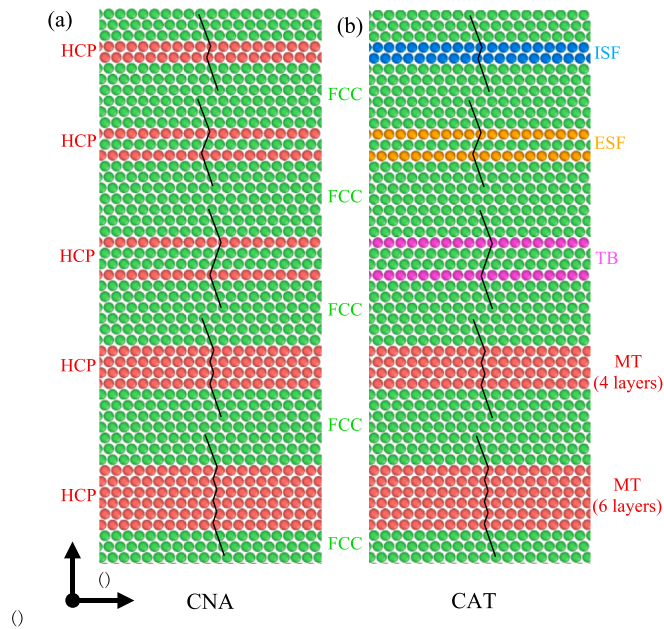


Fig. 2. Planar defects combined by HCP atoms. (a) Atom types identified by common neighborhood analysis (CNA). FCC and HCP atoms colored in green and red, respectively. (b) Planar defects of intrinsic stacking fault (ISF), extrinsic stacking fault (ESF), twin boundary (TB), and martensite structure (MT) identified by crystal-analysis-tool (CAT), colored in blue, yellow, pink, and red, respectively. (For interpretation of the references to color in this figure legend, the reader is referred to the web version of this article.)

GPa, which is near to the experimental value of 181.5 Gpa with grain size of 46.2 nm [61].

After the initial linear stage of stress-strain curves in Fig. 4, the stress increases up to different peaks and then drops. These stress peaks are known to be amplified due to the high strain rate generally employed in MD simulation, thus it is more meaningful to compare the average flow stress over a certain inelastic strain interval [16]. Fig. 5 shows the grain-size dependence of the average flow stress between 10 % and 20 % applied strain. It can be found that the average flow stress increases proportionally with reducing grain size up to a maximum value, satisfying the HP strengthening relationship. Then the average flow stress decreases with the further reduction of grain size, which is an IHP

softening relationship. The critical grain size (d_c) corresponding to the crossover from HP to IHP behavior is about $d_c \approx 27.31$ nm. This transition from HP strengthening to IHP softening with grain refinement in NiCoCrFe HEA is consistent with that in conventional alloys [14–21] and HEAs [22–29]. The experiment and simulation studies showed that the crossover from HP to IHP behavior with grain refinement in the nanocrystalline metals of Cu [14–16,18], Al [18,21], Ni [19] and Mg [20] occurs in the range of 10–20 nm, which corresponds to the transition of deformation mechanism from dislocation activity to grain boundary activity (slip, migration, merging and rotation, etc.). The experiment results on the NbMoTaW HEA with BCC structure exhibited the strongest grain size ~10 nm with the hardness of ~16.0 GPa, above which the hardness decreases with increasing the grain size or film thickness, while below this critical size the material softening occurs [25]. The simulation results showed that there also exists the HP relation and IHP relation in the Al_{0.1}CoCrFeNi HEA [26], and when grain size is higher than the critical grain size is about 14.77 nm, the deformation mechanism is the accumulation of dislocations at the grain boundaries, which conforms to the HP relation. At the case of grain diameter below the critical size, the migration of grain boundaries, amorphization of atoms as well as the rotation and merging of grains becomes the main deformation mechanism.

To further clarify the deformation mechanisms of the HP strengthening regime and IHP softening regime in the NiCoCrFe HEA, three samples with grain sizes of $d = 47.80$ nm, 27.31 nm, and 6.83 nm, corresponding to the strengthening, critical, and IHP softening regimes, respectively, are discussed in the following sections.

3.2. Microstructural evolutions in different deformation mechanisms

Fig. 6 shows the snapshots of atomic-scale microstructures during the uniaxial tension process of NiCoCrFe HEA with different grain sizes of $d = 47.80$ nm, 27.31 nm, and 6.83 nm. Meanwhile, the evolutions of statistical number of various microstructural configurations of GBs, dislocations, and planar defects (i.e., intrinsic stacking fault, extrinsic stacking fault, twin boundary and martensite phase) and are shown in Fig. 7. For the sample with large grain size of $d = 47.80$ nm in the HP strengthening regime, as shown in Fig. 6(a) and Fig. 7(a), some dislocations nucleate near GBs at about 5 % stain and then propagate across grains, leaving behind some intrinsic stacking faults (colored in blue). With the further increase of applied strain, more dislocations are formed, accompanied with the formation of various planar defects of intrinsic stacking fault, extrinsic stacking fault, twin boundary and

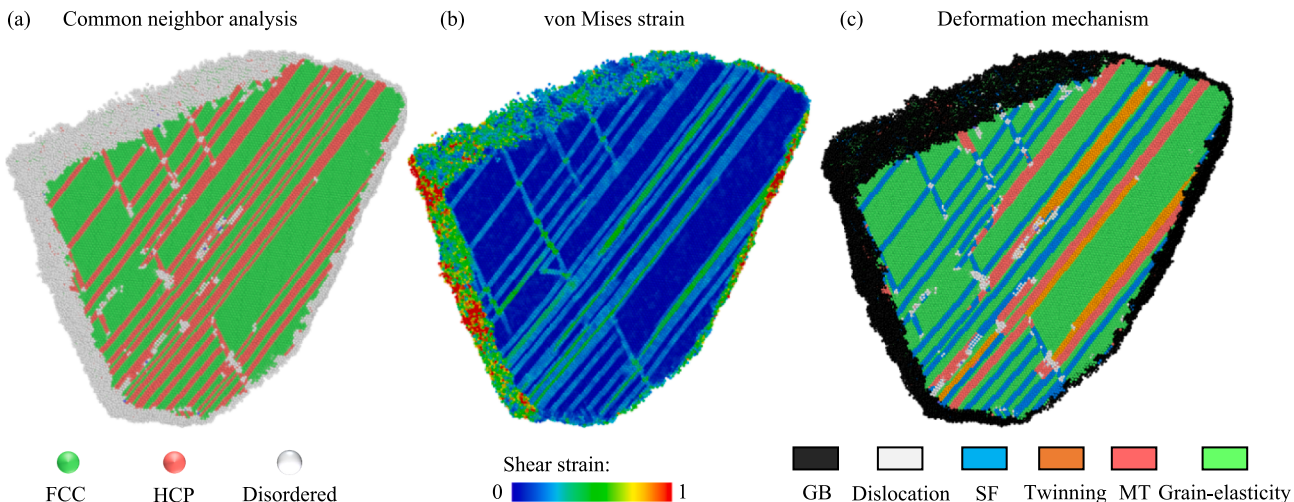


Fig. 3. Visualization of an arbitrary grain in NiCoCrFe high-entropy alloy with average grain size of 37.31 nm at 18 % applied strain. Atoms are colored according to (a) structure type identified by common neighborhood analysis (CNA), (b) von Mises strain, (c) deformation mechanisms of grain boundary activity (GB), dislocation, stacking fault (SF), twinning, martensite transformation (MT), and grain-elasticity.

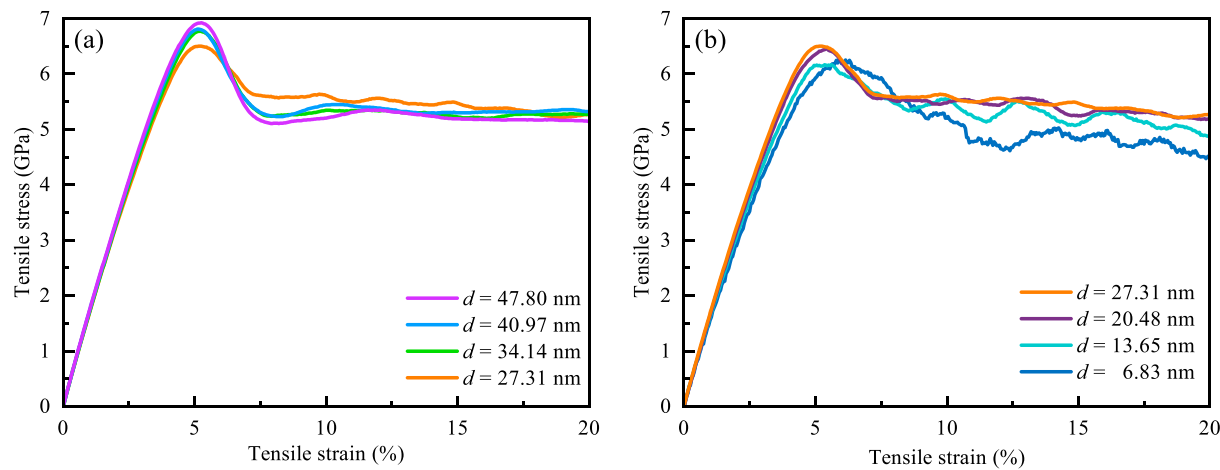


Fig. 4. Stress–strain curves of NiCoCrFe high-entropy alloy with various grain sizes (d) during uniaxial tension. (a) d : 47.80 nm–27.31 nm; (b) d : 27.31 nm–6.83 nm.

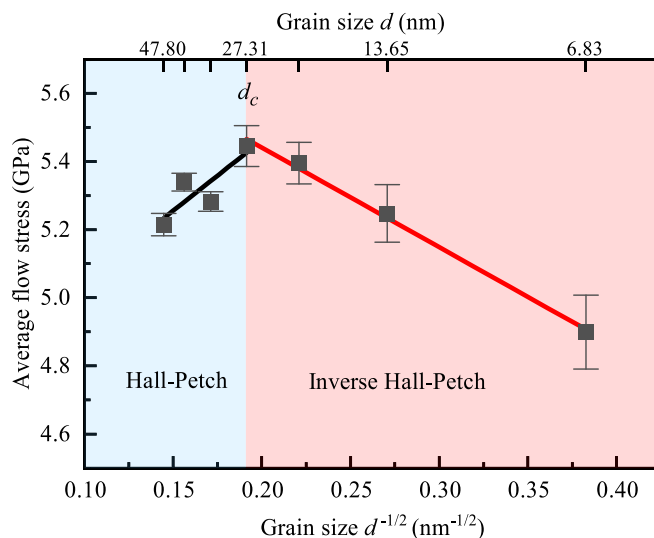


Fig. 5. Dependence of average flow stress with grain size in NiCoCrFe high-entropy alloy. Error bars characterize the standard deviation of fluctuation in the strain interval of 10 %–20 %.

martensite structure. Among these planar defects beside the intrinsic stacking fault, the martensite structure increases remarkably during the deformation process, while the extrinsic stacking fault and twin boundary both increase slightly. Just as the formation of massive planar defects with HCP atoms, the number of FCC atoms decreases quickly. At the 20 % applied strain, the proportions of intrinsic stacking faults and martensite phases reach to 16.3 % and 16.0 % of total atoms, respectively; while the extrinsic stacking faults and twin boundaries only occupy 3.2 % and 1.5 % of total atoms, respectively. This means that the planar defects of stacking fault and martensite phase both play a critical role in the HP strengthening regime of NiCoCrFe HEA, which have been observed in experiments [29,36,48].

From Fig. 6(a) and Fig. 7(a), it can also be found that the number of dislocation core atoms remains very small (no more than 3.0 %) in the whole deformation process, but the dislocation density continuously increases from 5 % applied strain, as shown in Fig. 8. Massive 1/6 $\langle 112 \rangle$ Shockley partial dislocations, bits of 1/6 $\langle 110 \rangle$ Stair-rod and 1/3 $\langle 100 \rangle$ Hirth dislocations are formed at 20 % applied strain, while the 1/2 $\langle 110 \rangle$ perfect dislocations are very few. Moreover, the proportion of GB atoms keeps no more than 6.9 % of total atoms during the deformation process, and the GB morphology maintains unchanged.

For the sample with critical grain size of $d_c = 27.31$ nm, as shown in

Fig. 6(b), Fig. 7(b), and Fig. 8, massive planar defects and lots of dislocations are formed during the deformation process, and they display the same evolution feature comparing with the sample in the HP strengthening regime ($d = 47.80$ nm). However, the dislocation density and the number of planar defects both are a bit smaller than the later sample, while the number of GB atoms enhances slightly.

For the sample with small grain size of $d = 6.83$ nm in the IHP softening regime, as shown in Fig. 6(c), Fig. 7(c), and Fig. 8, lots of intrinsic stacking faults and some martensite structures are formed during the deformation process, and they arrive to 12.6 % and 4.8 % of total atoms at the 20 % applied strain, respectively; while the extrinsic stacking faults and twin boundaries are both very few. And few dislocations are formed during the deformation process. However, the proportion of GB atoms increases from 26.1 % to 40.8 %, and the GBs widen remarkably. This means that the GBs accompanied with stacking faults and martensite structures play a critical role in the IHP softening regime of NiCoCrFe HEA.

In the HP strengthening and IHP softening regimes of NiCoCrFe HEA, the planar defects of stacking faults and martensite structures are much abundant than that in many traditional metals [14–21], which is attributed to the low stacking fault energy of NiCoCrFe HEA. The experiment results of stacking fault energy of NiCoCrFe HEA and Al, Ni, Cu traditional metals at 300 K are shown in Table 2, and the calculation results of Ni and NiCoCrFe are also shown using the code provided by Chen et al. [66]. As shown in Table 2, the stacking fault energy of NiCoCrFe HEA at 300 K in our simulation is much lower than that of Al, Ni, Cu traditional metals. Many experiments and calculations [30–38] have shown that the low stacking fault energy will promote the formation of stacking faults, twins, and martensite phases.

3.3. Formation mechanism of HCP-martensitic transformation

The HCP-martensitic transformation occurs in the deformation of NiCoCrFe HEA with different grain sizes, which has been widely observed in NiCoCrFe HEA at low temperature [36,48,67]. The FCC \rightarrow HCP phase transformation occurs via the nucleation and propagation of intrinsic stacking fault and the subsequent glide of dislocation on the intrinsic stacking fault, as shown in Fig. 9. The stacking sequence of FCC structure is labeled ABCABCABC. When a Shockley partial dislocation is activated on a (111) plane (e.g., the A plane in Fig. 9(a) marked with arrow), all atomic layers above the A plane will move by a vector of 1/6 $\langle 112 \rangle$. In this process, an intrinsic stacking fault is created, leading to a stacking sequence of ABCACABCAB. On the basis of the intrinsic stacking fault, gliding of a second Shockley partial dislocation on the second neighbor plane (e.g., the A plane in Fig. 9(b) marked with arrow), will form a four-layer HCP-martensite structure with the

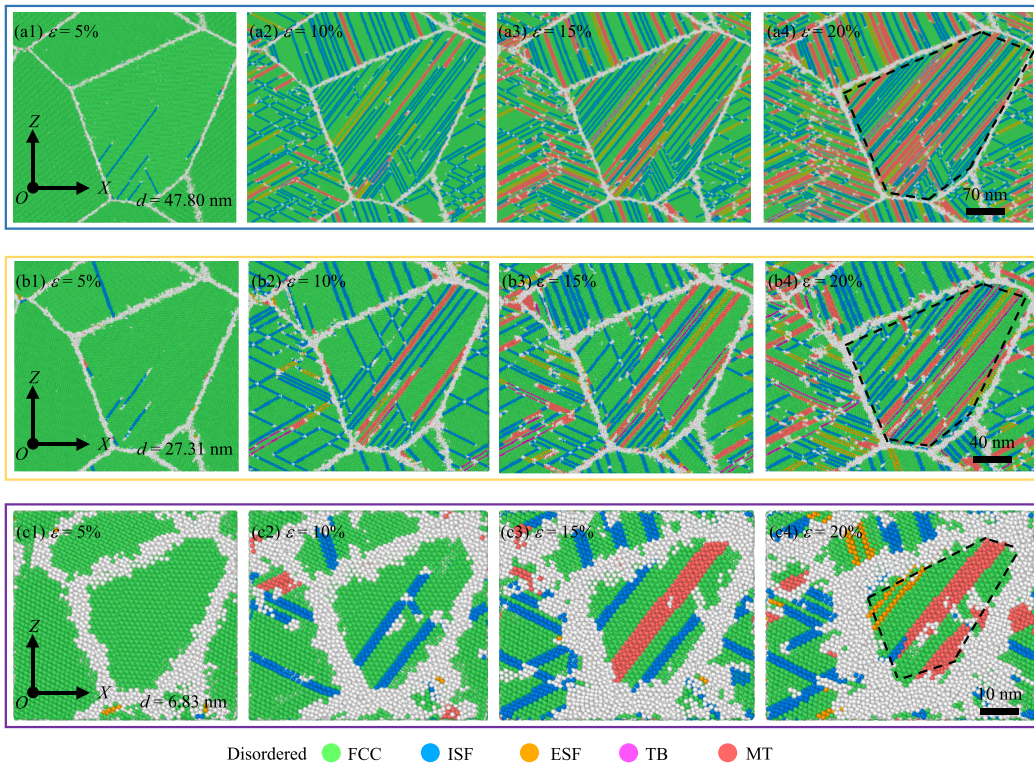


Fig. 6. Snapshots of atomic-scale microstructures during uniaxial tension process of NiCoCrFe high-entropy alloy with different grain sizes. (a1 ~ a4) $d = 47.80 \text{ nm}$; (b1 ~ b4) $d = 27.31 \text{ nm}$; (c1 ~ c4) $d = 6.83 \text{ nm}$. The disordered and FCC atoms are colored in white and green, respectively; the intrinsic stacking fault (ISF), extrinsic stacking fault (ESF), twin boundary (TB), and martensite structure (MT) are colored in blue, yellow, pink, and red, respectively. (For interpretation of the references to color in this figure legend, the reader is referred to the web version of this article.)

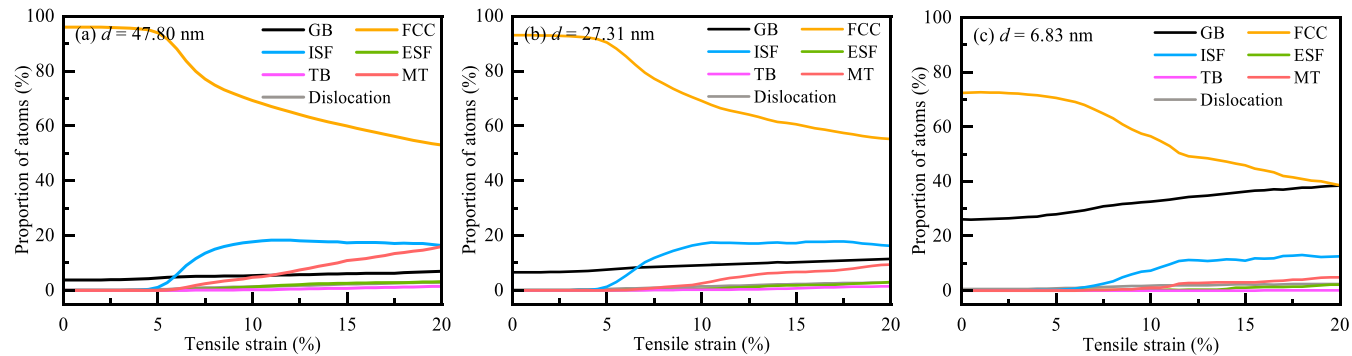


Fig. 7. Evolutions of statistical number of various microstructural configurations of GBs, dislocations, and planar defects of intrinsic stacking fault (ISF), extrinsic stacking fault (ESF), twin boundary (TB) and martensite structure (MT) during uniaxial tension process of NiCoCrFe high-entropy alloy with different grain sizes. (a) $d = 47.80 \text{ nm}$; (b) $d = 27.31 \text{ nm}$; (c) $d = 6.83 \text{ nm}$.

stacking sequence of ABCACACABC. Based on the four-layer HCP-martensite structure, successively gliding of Shockley partial dislocation, HCP-martensite structure with different thicknesses of HCP atomic layers can be formed, as shown in Fig. 9(c).

Fig. 10 shows the volume fraction and morphology of HCP-martensitic structures during the deformation process of NiCoCrFe HEA with different grain sizes. It can be found that more HCP-martensitic structures are formed in the sample with large grain size, and the thickness of martensitic structures is large. In the sample with large grain size ($d = 47.80 \text{ nm}$), the martensitic structures with 10-, 8-, and 6-layer HCP atoms are often observed, but no more than 4-layer HCP atoms is observed in the small grain size ($d = 6.83 \text{ nm}$). From Fig. 10, it can also be found that the initiation time of HCP-martensitic transformation in the samples with large grain sizes ($d > d_c: 27.31 \text{ nm}$) is remarkable earlier than that in the samples with small grain sizes ($d <$

$d_c: 27.31 \text{ nm}$). These results indicate that the large grain size favors the nucleation and growth of HCP-martensitic phases during the deformation of NiCoCrFe HEA, which is identical with the experimental results in the HEAs with transformation induced plasticity (TRIP) effect [28,67–70]. The experiments in $\text{Fe}_{40}\text{Co}_{20}\text{Cr}_{20}\text{Mn}_{10}\text{Ni}_{10}$ HEA showed that the initiation of HCP martensitic transformation occurred earlier in coarse-grain samples compared to fine-grain samples, along with the formation of much thicker and higher fraction of HCP plates [28]. The experimental results in NiCoCr medium-entropy alloy by Gu et al. [67] also demonstrated that the grain refinement strongly suppressed the deformation-induced martensitic transformation. Some studies [68–70] have shown the grain-size dependence of deformation-induced martensitic transformation is attributed to the reduction of apparent stacking fault energy with increasing grain size.

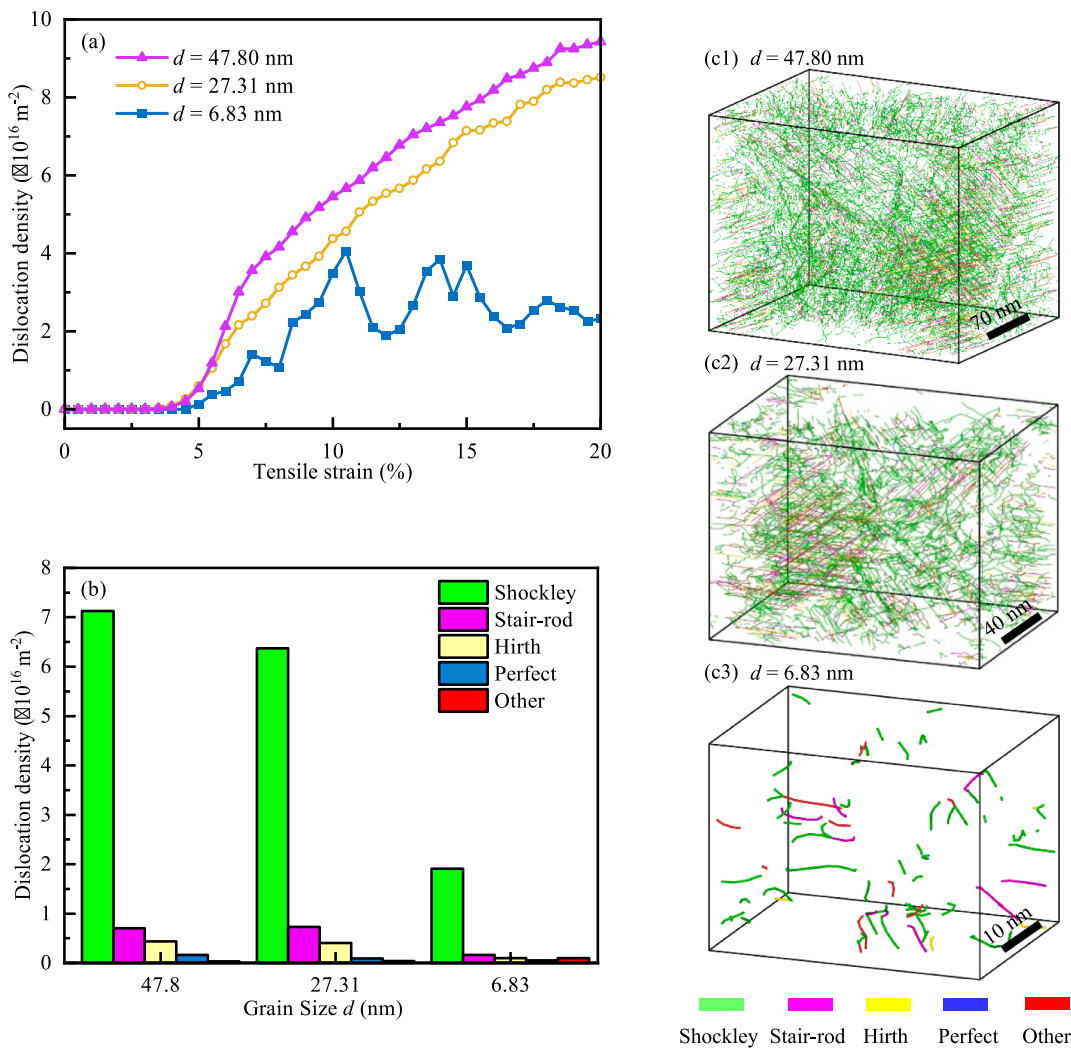


Fig. 8. Dislocation in NiCoCrFe high-entropy alloy with different grain sizes of $d = 47.80 \text{ nm}$, 27.31 nm and 6.83 nm . (a) Evolutions of dislocation density during uniaxial tension process. (b) Statistical number and (c) spatial distribution of various dislocations at 20 % strain. Shockley partial dislocation, stair-rod dislocation, Hirth dislocation, and perfect dislocation are shown in green, purple, yellow, and blue colors, respectively, while others are shown in red color. (For interpretation of the references to color in this figure legend, the reader is referred to the web version of this article.)

Table 2
Stacking fault energy (γ_{SF}) of NiCoCrFe high-entropy alloy and Al, Ni, Cu traditional metals at 300 K.

Alloy	Stacking fault energy (mJ/m^2)	
	Experiment	Calculation
Al	120–144 [62]	\
Ni	125 [63]	133.32
Cu	45 [64]	\
NiCoCrFe	23–32 [65]	8.62

3.4. Grain-size dependence of grain boundary activities

Many experiments and simulations have revealed that the GBs in ultrafine-grained metals play a key role in its plasticity [15–19]. The activities of disordered GB atoms such as GB migration and sliding mainly contribute to the nonaffine plastic displacement [71], and it can be quantified by the nonaffine squared atomic rearrangement

$$D_{\min}^2 = \min_{F^a} \sum_{\beta=1}^{N_a} |x^{\alpha\beta} - F^a X^{\alpha\beta}|^2 \quad (4)$$

Fig. 11 shows the grain-size dependences of GB activities in NiCrCoFe HEA. For the samples with large grain size ($d > d_c: 27.31 \text{ nm}$) in the HP strengthening regime, the nonaffine square displacement D_{\min}^2 is small and increase slightly with reducing grain size, and the migration of GBs is very weak during the deformation process as shown in **Fig. 11 (b)**. Below the critical grain size ($d < d_c: 27.31 \text{ nm}$) in the IHP softening regime, the nonaffine square displacement D_{\min}^2 increases rapidly, and the GBs undergoes a significant migration during the deformation process. This suggests that the GB activities play an important role in the IHP softening regime.

4. Quantitative description of multiple deformation mechanisms

To quantitatively analyze the contribution of various microstructural configurations to the multiple deformation mechanisms in NiCrCoFe HEA, the evolutions of atomic shear strain in NiCoCrFe HEA with different grain sizes of $d = 47.80 \text{ nm}$, 27.31 nm , and 6.83 nm are shown in **Fig. 12**. The atoms are colored according to their local von Mises shear strain, and the red color represents the high shear strain. For the sample with large grain size of $d = 47.80 \text{ nm}$ in the HP strengthening regime, as shown in **Fig. 12(a1-a4)**, the GB atoms have high shear strain during

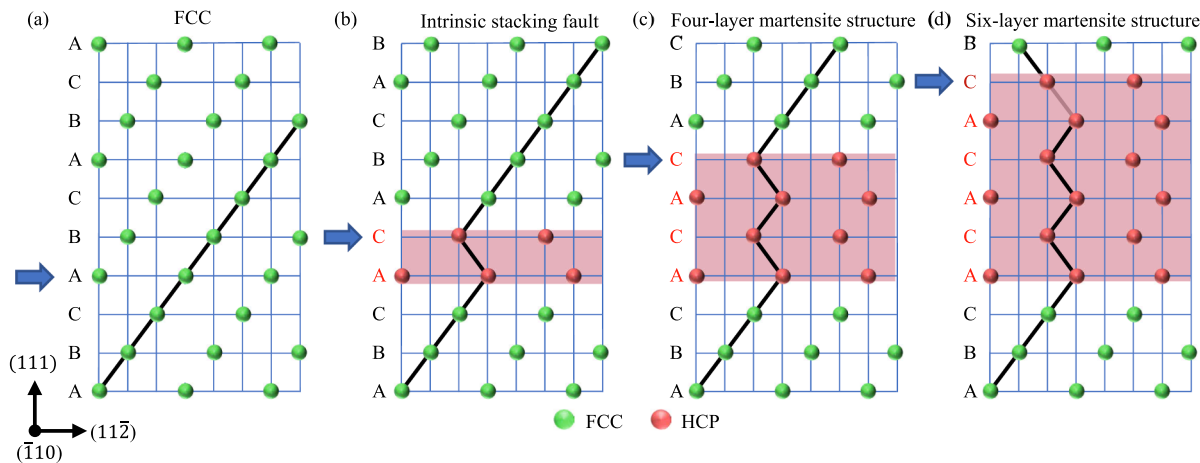


Fig. 9. Schematic illustrating the formation process of HCP-martensitic structure from FCC structure. (a) FCC; (b) Intrinsic stacking fault; (c) Four-layer martensite structure; (d) Six-layer martensite structure.

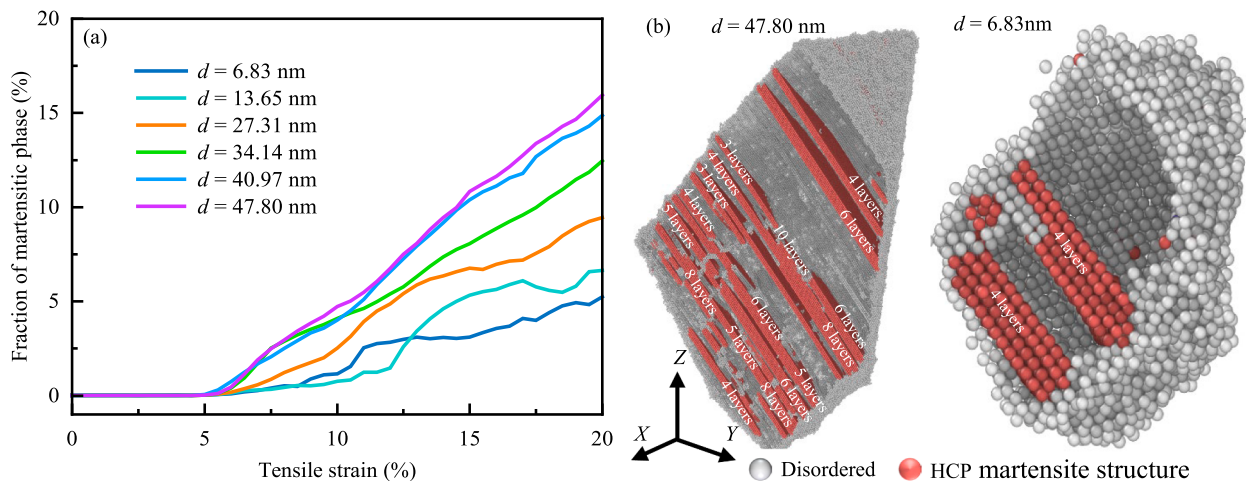


Fig. 10. Martensitic structures in NiCoCrFe high-entropy alloy with different grain sizes. (a) Evolution of the fraction of martensitic phases during uniaxial tension process. (b) Morphology of martensitic structures in the samples with large grain size ($d = 47.80 \text{ nm}$) and small grain size ($d = 6.83 \text{ nm}$) at applied tensile strain of 20 %. The thickness of the martensitic structure with various layer of HCP atoms are labeled. Only HCP atoms and disordered atoms are shown for clarity.

deformation process. With the formation of various planar defects, the shear strain of intragranular atoms increases remarkably. Thereinto, the stair-rod dislocations indicated by the dashed ellipses have the highest shear strain, then is the twin boundaries, martensite phases, and stacking faults on turn. For the sample with small grain size of $d = 6.83 \text{ nm}$ in the IHP softening regime, as shown in Fig. 12(c1-c4), the shear strain of GB atoms keeps higher than that of intragranular atoms during the deformation process, though some dislocations and various planar defects are formed.

Fig. 13 further shows the percentages of total strain accommodated by different deformation mechanisms p_k (i.e. GB activity, dislocation, stacking fault, twinning, and martensite transformation) during the flow of NiCoCrFe HEA with different grain sizes. In the HP strengthening regime ($d > d_c: 27.31 \text{ nm}$), at the initial flow (10 % applied strain), the stacking faults accommodate the largest amount of strain (more than 34.1 %), governing the deformation response; the GBs accommodate a significant amount of strain (more than 23.4 %); the martensite phases also accommodate some strains (more than 8.0 %); but the contribution of twin boundaries and dislocations is very small (no more than 3.4 %). With continued loading (20 % applied strain), the total strain of stacking faults decreases while the martensite phases increase remarkably, as some stacking faults transform into martensite structures during the

flow process. Meanwhile, the distributions of GBs, twin boundaries, and dislocations all increase slightly. This means that the deformation in the HP strengthening regime of NiCoCrFe HEA are dominated by multiple mechanisms of stacking fault, GB activity, and HCP martensitic transformation, accompanied with twinning and dislocation, and the role of HCP martensitic transformation enhances during the flow process. It should be noted that although the proportion of GB atoms keeps no more than 6.9 % of total atoms during the deformation process, as shown in Fig. 7(a), its contribution to the total deformation is significant due to the high shear strain of each GB atoms (see Fig. 12(a)). The dislocation cores also have high shear strain (see Fig. 12 (a)), but its contribution to the total deformation is rather small as the extremely small proportion of dislocation core atoms (no more than 3.0 %).

In the IHP softening regime ($d < d_c: 27.31 \text{ nm}$), the GBs accommodate the largest amount of strain (more than 34.9 %) at the initial flow (10 % applied strain) and it further enhances with continued loading, governing the deformation response. The stacking faults also accommodate a significant amount of strain (more than 19.5 %) during the flow and slightly decreases with continued loading, but the contributions of twin boundaries, martensite phases, but dislocations are extremely small (no more than 4.3 %). This means that the deformation mechanisms in the IHP strengthening regime of NiCoCrFe HEA are

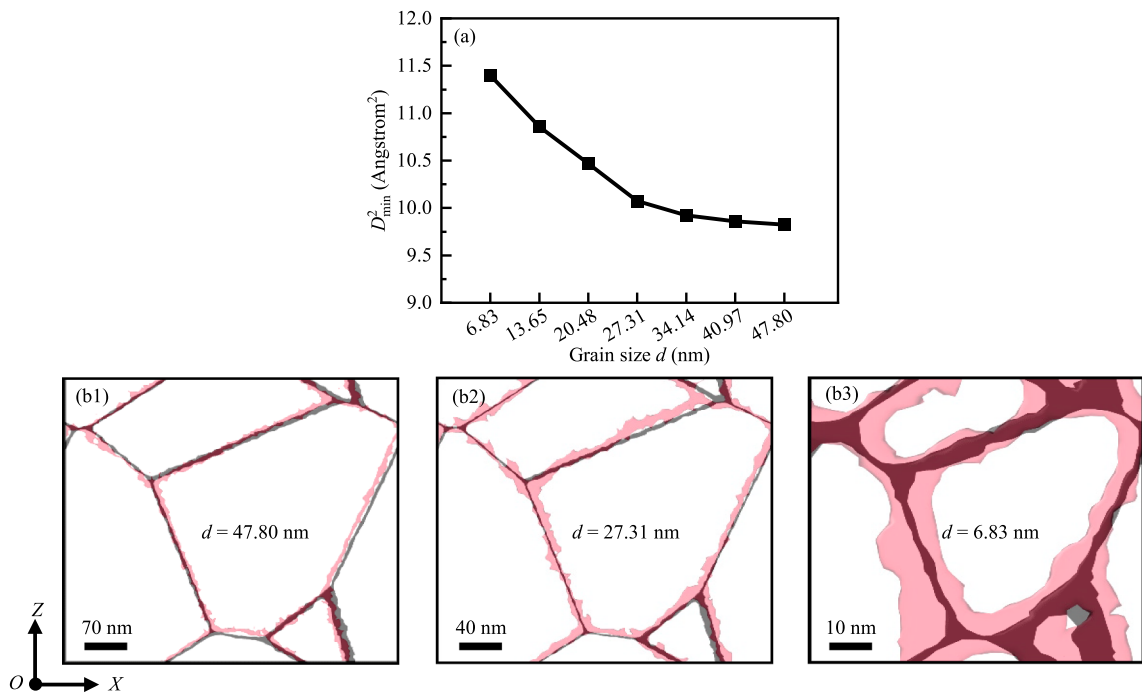


Fig. 11. Grain-size dependences of grain boundary activities in NiCoCrFe high-entropy alloy. (a) Evolution of nonaffine displacement D_{\min}^2 with grain size under 20 % applied strain. (b) Migration of grain boundaries under 20 % applied strain in the samples with three typical grain sizes of 47.80 nm, 27.31 nm, and 6.83 nm, respectively.

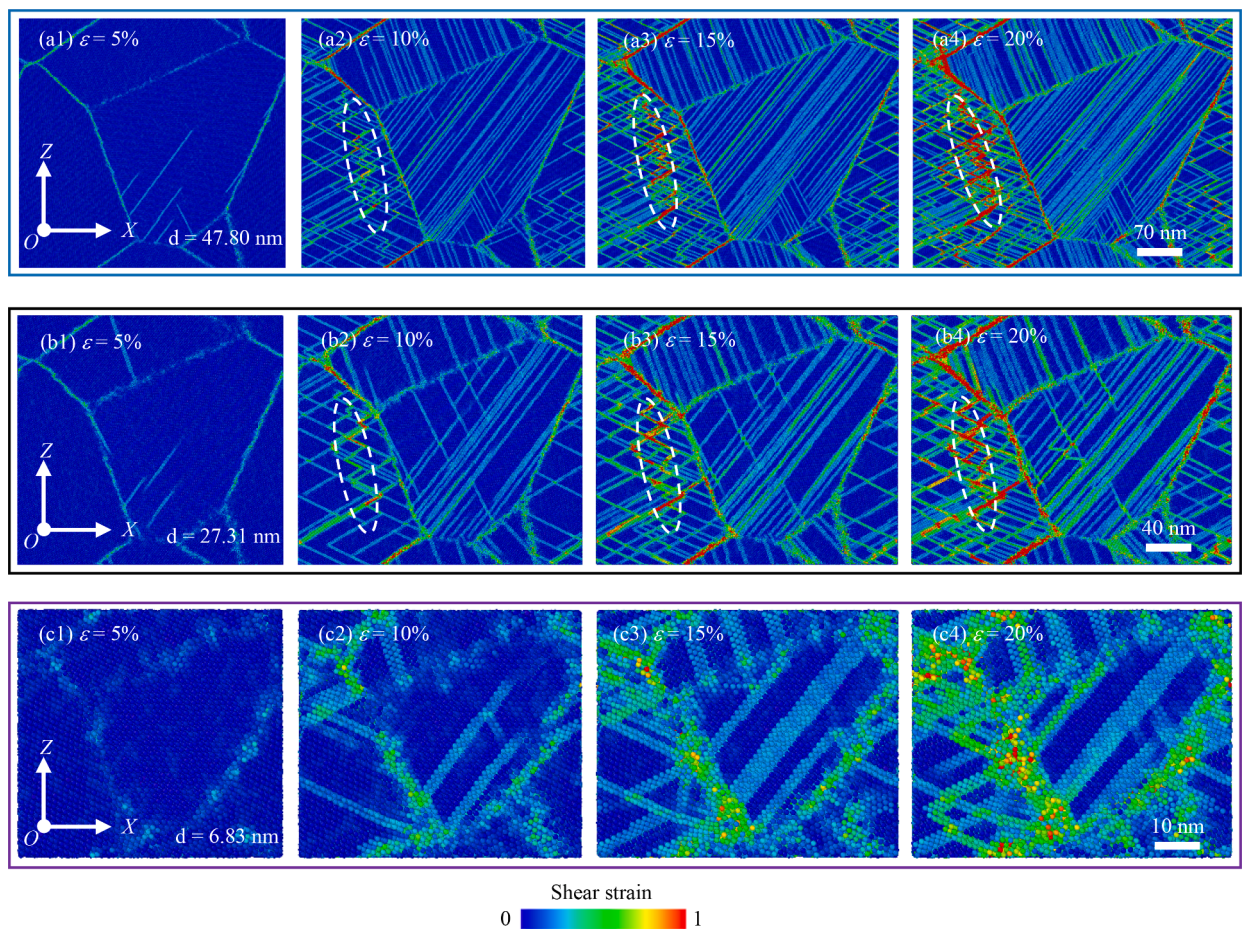


Fig. 12. Snapshots of atomic shear strain of NiCoCrFe high-entropy alloy with different grain sizes during uniaxial tension process. (a1 ~ a4) $d = 47.80$ nm; (b1 ~ b4) $d = 27.31$ nm; (c1 ~ c4) $d = 6.83$ nm.

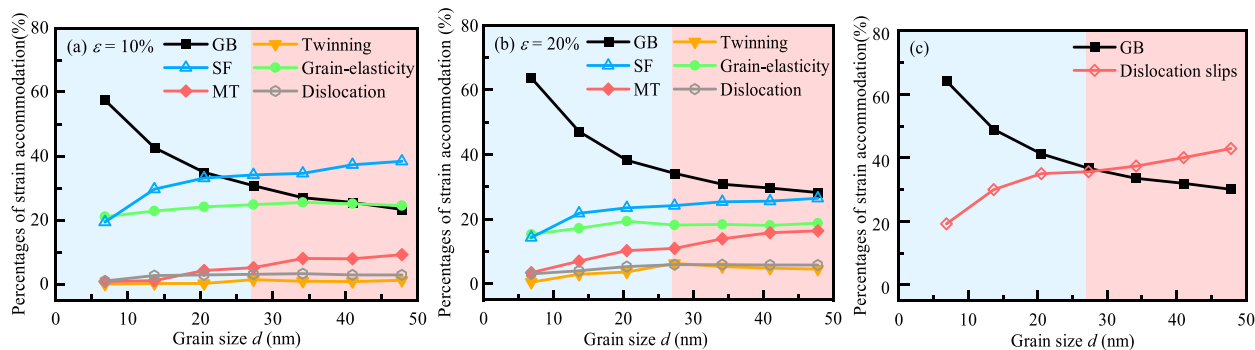


Fig. 13. Grain size dependence of strain accommodated by different deformation mechanisms of grain boundary activity (GB), dislocation, stacking fault (SF), twinning, martensite transformation (MT), and grain-elasticity in NiCoCrFe high-entropy alloy at different flow stages. (a) 10% applied strain, (b) 20% applied strain, (c) averaged over 10%–20% applied strain.

dominated by GB activity and stacking fault.

The grain-elastic contribution to overall deformation is comparatively large in the flow process, as shown in Fig. 13 (a-b), which is expected to be higher in nanocrystalline metals than that of their coarser-grained counterparts [44,45]. It can also be found that the strain accommodated by grain-elasticity is independent of grain size, this suggests that the grain-elasticity does not participate in competing among different deformation mechanisms.

The planar defects of intrinsic stacking fault, extrinsic stacking fault, twin boundary, and martensite structure all come from the slipping of partial dislocation (see Fig. 9). Thus, the deformation mechanisms of stacking fault, twinning, martensite transformation, and dislocation can be classified into dislocation slip. Fig. 13(c) shows the grain-size dependence of the percentage of total strain accommodated by all dislocation slips averaged over 10 %–20 % applied strain. Here, the strain interval in calculating the strain accommodation is consistent with that in calculating the average flow stress shown in Fig. 5. It can be found that the deformation mechanism in the HP strengthening regime is dominated by dislocation slips, accompanied with GB activities. The dominant deformation mechanism transforms from dislocation slips to GB activities with reducing grain size, and the cross-over just corresponds to the critical grain size determined by grain-size dependence of average flow stress (see Fig. 5), which verifies the effectiveness in quantitatively analyzing the multiple deformation mechanisms of NiCr-CoFe HEA. It should be noted that the deformation mechanism of dislocation slips here includes multiple deformation mechanisms of dislocation, stacking fault, twinning, and martensitic transformation, but not just the dislocation and accompanied intrinsic stacking fault in conventional alloys [14–21].

5. Conclusions

The tensile process of NiCoCrFe HEA with different grain sizes is simulated by MD method to quantitatively describe the multiple deformation mechanisms. The contributions of various deformation mechanisms to the total deformation, including GB activity, dislocation, twinning, stacking fault, and FCC → HCP martensitic transformation, are systematically studied by means of post-processing metrics. The grain-size dependent mechanical behavior and the competitions of various deformation mechanisms with grain refinement are revealed. The major findings are summarized as follows.

The average flow stress increases proportionally with reducing grain size up to a maximum value, satisfying the HP strengthening relationship. Then the average flow stress decreases with the further reduction of grain size, which is an IHP softening relationship. The critical grain size (d_c) corresponding to the crossover from HP to IHP behavior is about $d_c \approx 27.31$ nm.

In the HP strengthening regime ($d > d_c$), beside many 1/6 {112}

Shockley partial dislocations, massive planar defects of intrinsic stacking faults and martensite structures are formed during the deformation process, which have been widely observed in experiments. In the IHP softening regime ($d < d_c$), beside the dominant GBs, lots of intrinsic stacking faults and some martensite structures are formed during the deformation process. More planar defects of stacking fault, martensite structure, and twin boundary are formed in the deformation of NiCrCoFe HEA comparing with most traditional metals, which is attributed to its low stacking fault energy.

The FCC → HCP phase transformation in the deformation of NiCoCrFe HEA occurs via the nucleation and propagation of intrinsic stacking fault and the subsequent glide of dislocation on the intrinsic stacking fault. And the large grain size favors the nucleation and growth of HCP-martensitic phases during the deformation of NiCoCrFe HEA.

Multiple deformation mechanisms are found in the HP strengthening and IHP softening regimes of NiCoCrFe HEA by quantitatively analyzing the contribution of various microstructural configurations to deformation. In the HP strengthening regime, the deformation mechanisms are dominated by stacking fault, GB activity, and HCP martensitic transformation, accompanied with twinning and dislocation. In the IHP softening regime, the deformation mechanisms are dominated by GB activity and stacking fault. The deformation mechanisms revealed according to the percentages of total strain accommodated by various microstructural configurations is more accurate than their atomic fractions.

CRediT authorship contribution statement

Jun Chen: Writing – original draft, Software, Methodology, Investigation, Data curation. **Zhaoyang Hou:** Writing – review & editing, Methodology, Funding acquisition, Conceptualization. **Zhen Wang:** Visualization, Software, Data curation. **Kefan Li:** Software, Data curation. **Pengfei Zou:** Writing – review & editing. **Kejun Dong:** Writing – review & editing. **Gang Shi:** Project administration, Conceptualization.

Declaration of competing interest

The authors declare that they have no known competing financial interests or personal relationships that could have appeared to influence the work reported in this paper.

Data availability

No data was used for the research described in the article.

Acknowledgments

The authors would like to acknowledge the Natural Science Basis

Research Plan in Shaanxi Province of China (2023JCYB445). This work is also supported by the Fundamental Research Funds for the Central Universities of CHD (Grant Nos. 300102122201, 300102122106).

References

- [1] J.-W. Yeh, S.-K. Chen, S.-J. Lin, J.-Y. Gan, T.-S. Chin, T.-T. Shun, C.-H. Tsau, S.-Y. Chang, Nanostructured high-entropy alloys with multiple principal elements: novel alloy design concepts and outcomes, *Adv. Eng. Mater.* 6 (2004) 299–303.
- [2] B. Cantor, I.T.H. Chang, P. Knight, A.J.B. Vincent, Microstructural development in equiatomic multicomponent alloys, *Mater. Sci. Eng. A* 375–377 (2004) 213–218.
- [3] D.B. Miracle, O.N. Senkov, A critical review of high entropy alloys and related concepts, *Acta Mater.* 122 (2017) 448–511.
- [4] E.P. George, D. Raabe, R.O. Ritchie, High-entropy alloys, *Nat. Rev. Mater.* 4 (2019) 515–534.
- [5] P. Sathiyamoorthi, H.S. Kim, High-entropy alloys with heterogeneous microstructure: processing and mechanical properties, *Prog. Mater Sci.* 123 (2022) 100709.
- [6] Y. Zhang, T.T. Zuo, Z. Tang, M.C. Gao, K.A. Dahmen, P.K. Liaw, Z.P. Lu, Microstructures and properties of high-entropy alloys, *Prog. Mater Sci.* 61 (2014) 1–93.
- [7] J. Chen, X.Y. Zhou, W.L. Wang, B. Liu, Y.K. Lv, W. Yang, D.P. Xu, Y. Liu, A review on fundamental of high entropy alloys with promising high-temperature properties, *J. Alloys Compd.* 760 (2018) 15–30.
- [8] W.D. Li, D. Xie, D.Y. Li, Y. Zhang, Y.F. Gao, P.K. Liaw, Mechanical behavior of high-entropy alloys, *Prog. Mater Sci.* 118 (2021) 100777.
- [9] J. Li, X.B. Fu, H. Feng, B. Liu, P.K. Liaw, Q.H. Fang, Evaluating the solid solution, local chemical ordering, and precipitation strengthening contributions in multi-principal-element alloys, *J. Alloys Compd.* 938 (2023) 168521.
- [10] R. Ren, J.F. Fan, B.S. Wang, Q. Zhang, W.G. Li, H.B. Dong, Hall-Petch relationship and deformation mechanism of pure Mg at room temperature, *J. Alloys Compd.* 920 (2022) 165924.
- [11] S.N. Naik, S.M. Walley, The Hall-Petch and inverse Hall-Petch relations and the hardness of nanocrystalline metals, *J. Mater. Sci.* 55 (2019) 2661–2681.
- [12] E.O. Hall, The deformation and ageing of mild steel. III discussion of results, *Proc. Phys. Soc., London.* 64 (1951) 747–753.
- [13] N.J. Petch, The cleavage strength of polycrystals, *J. Iron Steel Inst., London* 174 (1953) 25–28.
- [14] E.N. Hahn, M.A. Meyers, Grain-size dependent mechanical behavior of nanocrystalline metals, *Mater. Sci. Eng. A* 646 (2015) 101–134.
- [15] V. Yamakov, D. Wolf, S.R. Phillipot, A.K. Mukherjee, H. Gleiter, Deformation-mechanism map for nanocrystalline metals by molecular-dynamics simulation, *Nat. Mater.* 3 (2003) 43–47.
- [16] J. Schiøtz, K.W. Jacobsen, A maximum in the strength of nanocrystalline copper, *Science* 301 (2003) 1357–1359.
- [17] J. Hu, Y.N. Shi, X. Sauvage, G. Sha, K. Lu, Grain boundary stability governs hardening and softening in extremely fine nanograined metals, *Science* 355 (2017) 1292–1296.
- [18] L. Zhang, C. Lu, K. Tieu, A review on atomistic simulation of grain boundary behaviors in face-centered cubic metals, *Comput. Mater. Sci.* 118 (2016) 180–191.
- [19] S. Zhou, Z.Y. Hou, N.N. Liu, Y. Niu, C. Li, Z. Wang, J.G. Wang, L. Gao, K.J. Dong, Optimal grain size distribution in gradient nano-grained nickel, *Vacuum* 210 (2023) 111854.
- [20] Y.F. Bu, X.Z. Zhang, D.S. Zhou, Unraveling the strain-dependent Hall-Petch slope in low-to-high Mg content Al-Mg alloys, *J. Alloys Compd.* 963 (2023) 171238.
- [21] Z.Y. Hou, S. Zhou, Y. Niu, F.L. Wang, P.F. Zou, G. Shi, L. Gao, K.J. Dong, Effect of twin spacing on the mechanical behavior and deformation mechanism of nanotwinned Al, *Mater. Sci. Eng. a.* 862 (2023) 144465.
- [22] J. Yang, J.W. Qiao, S.G. Ma, G.Y. Wu, D. Zhao, Z.H. Wang, Revealing the Hall-Petch relationship of Al_{0.1}CoCrFeNi high-entropy alloy and its deformation mechanisms, *J. Alloys Compd.* 795 (2019) 269–274.
- [23] L.C. Chang, Y.C. Lu, C.H. Hsueh, Effects of aluminum addition on microstructures and mechanical properties of NbTiVZr high-entropy alloy nitride films, *Intermetallics* 156 (2023) 107868.
- [24] S. Guo, S. Sui, M. Wang, X.H. Hao, H. Chen, C.Z. Wang, B.X. Huang, X. Lin, Overcoming strength-ductility trade-off in high-entropy alloys by tuning chemical short-range order and grain size, *Intermetallics* 150 (2022) 107693.
- [25] X.B. Feng, J.Y. Zhang, Y.Q. Wang, Z.Q. Hou, K. Wu, G. Liu, J. Sun, Size effects on the mechanical properties of nanocrystalline NbMoTaW refractory high entropy alloy thin films, *Int. J. Plast.* 95 (2017) 264–277.
- [26] J. Jiang, W.F. Sun, N. Luo, Atomic insights into effects of temperature and grain diameter on the micro-deformation mechanism, mechanical properties and sluggish diffusion of nanocrystalline high-entropy alloys, *Mater. Today Commun.* 33 (2022) 104224.
- [27] M. Schneider, G. Laplanche, Effects of temperature on mechanical properties and deformation mechanisms of the equiatomic CrFeNi medium-entropy alloy, *Acta Mater.* 204 (2021) 116470.
- [28] W.T. Chen, X.L. An, Z.W. Wang, Y. Li, J. Gu, M. Song, Grain size dependent deformation behavior of a metastable Fe₄₀Co₂₀Cr₂₀Mn₁₀Ni₁₀ high-entropy alloy, *J. Alloys Compd.* 883 (2021) 160876.
- [29] X.R. Liu, S.H. Jiang, J.L. Lu, J. Wei, D.X. Wei, F. He, The dual effect of grain size on the strain hardening behaviors of Ni-Co-Cr-Fe high entropy alloys, *J. Mater. Sci. Technol.* 131 (2022) 177–184.
- [30] F. Otto, A. Dlouhý, C. Somsen, H. Bei, G. Eggeler, E.P. George, The influences of temperature and microstructure on the tensile properties of a CoCrFeMnNi high-entropy alloy, *Acta Mater.* 61 (2013) 5743–5755.
- [31] S.J. Chen, H.S. Oh, B. Gludovatz, S.J. Kim, E.S. Park, Z. Zhang, R.O. Ritchie, Q. Yu, Real-time observations of TRIP-induced ultrahigh strain hardening in a dual-phase CrMnFeCoNi high-entropy alloy, *Nat. Commun.* 11 (2020) 826.
- [32] D.X. Wei, X.Q. Li, S. Schönecker, J. Jiang, W.M. Choi, B.J. Lee, H.S. Kim, A. Chiba, H. Kato, Development of strong and ductile metastable face-centered cubic single-phase high-entropy alloys, *Acta Mater.* 181 (2019) 318–330.
- [33] D.X. Wei, X.Q. Li, J. Jiang, W.C. Heng, Y. Koizumi, W.M. Choi, B.J. Lee, H.S. Kim, H. Kato, A. Chiba, Novel Co-rich high performance twinning-induced plasticity (TWIP) and transformation-induced plasticity (TRIP) high-entropy alloys, *Scr. Mater.* 165 (2019) 39–43.
- [34] H.Y. He, M. Naeem, F. Zhang, Y.L. Zhao, S. Harjo, T. Kawasaki, B. Wang, X.L. Wu, S. Lan, Z.D. Wu, W. Yin, Y. Wu, Z.P. Lu, J.J. Kai, C.T. Liu, X.L. Wang, Stacking fault driven phase transformation in CrCoNi medium entropy alloy, *Nano Lett.* 21 (2021) 1419–1426.
- [35] L. Li, Z.H. Chen, S. Kuroiwa, M. Ito, K. Kishida, H. Inui, E.P. George, Tensile and compressive plastic deformation behavior of medium-entropy Cr-Co-Ni single crystals from cryogenic to elevated temperatures, *Int. J. Plast.* 148 (2022) 103144.
- [36] M. Naeem, H.Y. He, F. Zhang, H.L. Huang, S. Harjo, T. Kawasaki, B. Wang, S. Lan, Z.D. Wu, F. Wang, Y. Wu, Z.P. Lu, Z.W. Zhang, C.T. Liu, X.L. Wang, Cooperative deformation in high-entropy alloys at ultralow temperatures, *Sci. Adv.* 6 (2020) eaax4002.
- [37] L. Li, H.T. Chen, Q.H. Fang, J. Li, F. Liu, Y. Liu, P.K. Liaw, Effects of temperature and strain rate on plastic deformation mechanisms of nanocrystalline high-entropy alloys, *Intermetallics* 120 (2020) 106741.
- [38] Z.M. Pan, Y. Fu, Y. Wei, X.B. Yan, H. Luo, X.G. Li, Deformation mechanisms of TRIP-TWIP medium-entropy alloys via molecular dynamics simulations, *Int. J. Mech. Sci.* 219 (2022) 107098.
- [39] R.G. Liu, J. Tang, J.X. Jiang, X.Y. Li, Y.J. Wei, Stacking fault induced hardening and grain size effect in nanocrystalline CoNiCrFeMn high-entropy alloy, *Extreme Mech. Lett.* 56 (2022) 101875.
- [40] C. Yang, Y.C. Liang, L.L. Zhou, Q. Chen, B. Wang, L. Zhang, J.J. Ma, T.H. Gao, Q. Xie, Study on mechanical properties of high-entropy crystal/amorphous composites with pre-existing hole, *J. Alloys Compd.* 959 (2023) 170565.
- [41] D.E. Spearot, G.J. Tucker, A. Gupta, G.B. Thompson, Mechanical properties of stabilized nanocrystalline FCC metals, *J. Appl. Phys.* 126 (2019) 110901.
- [42] G.J. Tucker, S. Tiwari, J.A. Zimmerman, D.L. McDowell, Investigating the deformation of nanocrystalline copper with microscale kinematic metrics and molecular dynamics, *J. Mech. Phys. Solids.* 60 (2012) 471–486.
- [43] G.J. Tucker, J.A. Zimmerman, D.L. McDowell, Continuum metrics for deformation and microrotation from atomistic simulations: application to grain boundaries, *Int. J. Eng. Sci.* 49 (2011) 1424–1434.
- [44] A. Gupta, J. Gruber, S.S. Rajaram, G.B. Thompson, D.L. McDowell, G.J. Tucker, On the mechanistic origins of maximum strength in nanocrystalline metals, *npj Comput. Mater.* 6 (2020) 153.
- [45] A. Gupta, W.R. Jian, S.Z. Xu, I.J. Beyerlein, G.J. Tucker, On the deformation behavior of CoCrNi medium entropy alloys: unraveling mechanistic competition, *Int. J. Plast.* 159 (2022) 103442.
- [46] B. Gludovatz, A. Hohenwarter, D. Catoor, E.H. Chang, E.P. George, R.O. Ritchie, A fracture-resistant high-entropy alloy for cryogenic applications, *Science* 345 (2014) 1153–1158.
- [47] B. Gludovatz, A. Hohenwarter, K.V.S. Thurston, H.B. Bei, Z.G. Wu, E.P. George, R.O. Ritchie, Exceptional damage-tolerance of a medium-entropy alloy CrCoNi at cryogenic temperatures, *Nat. Commun.* 7 (2016) 10602.
- [48] W.C. Zhong, S. Hayakawa, H.X. Xu, K. An, A.Y. Borisevich, J.L. Cicotte, E.P. George, Y. Yang, Deciphering the multiple deformation mechanisms responsible for sustained work hardening in a FeCrCoNi medium entropy alloy, *Int. J. Plast.* 167 (2023) 103663.
- [49] S. Plimpton, Fast parallel algorithms for short-range molecular dynamics, *J. Comput. Phys.* 117 (1995) 1–19.
- [50] W.M. Choi, Y.H. Jo, S.S. Sohn, S. Lee, B.J. Lee, Understanding the physical metallurgy of the CoCrFeMnNi high-entropy alloy: an atomistic simulation study, *npj Comput. Mater.* 4 (2018) 1.
- [51] D.X. Cui, J.B. Zhang, X. Li, Z. Liang, X. Zhang, Y. Yang, H.F. Wang, Atomistic insights into sluggish crystal growth in an undercooled CoNiCrFe multi-principal element alloy, *J. Alloys Compd.* 941 (2023) 168881.
- [52] R.N. Li, H.Y. Song, M.X. Xiao, M.R. An, Atomic-scale insight into interaction mechanism between screw dislocation and HCP phase in high-entropy alloy, *J. Appl. Phys.* 133 (2023) 034302.
- [53] Z.W. Chen, R. Wang, Y. Shu, Y.P. Lin, Z.X. Liu, H.Q. Deng, W.Y. Hu, T.F. Yang, The interactions between dislocations and displacement cascades in FeCoCrNi concentrated solid-solution alloy and pure Ni, *J. Nucl. Mater.* 576 (2023) 154286.
- [54] Y.Q. Tang, D.Y. Li, Dynamic response of high-entropy alloys to ballistic impact, *Sci. Adv.* 8 (2022) eabp9096.
- [55] D. Utt, S. Lee, Y.L. Xing, H. Jeong, A. Stukowski, S.H. Oh, G. Dehm, K. Albe, The origin of jerky dislocation motion in high-entropy alloys, *Nat. Commun.* 13 (2022) 4777.
- [56] R. Gröger, V. Vitek, A. Dlouhý, Effective pair potential for random fcc CoCrFeMnNi alloys, *Modell. Simul. Mater. Sci. Eng.* 28 (2020) 075006.
- [57] Y. Tong, K. Jin, H. Bei, J.Y.P. Ko, D.C. Pagan, Y. Zhang, F.X. Zhang, Local lattice distortion in NiCo₂Cr, FeCoNiCr and FeCoNiCrMn concentrated alloys investigated by synchrotron X-ray diffraction, *Mater. Des.* 155 (2018) 1–7.
- [58] J.D. Honeycutt, H.C. Andersen, Molecular dynamics study of melting and freezing of small Lennard-Jones clusters, *J. Phys. Chem.* 91 (1987) 4950–4963.

- [59] A. Stukowski, Computational analysis methods in atomistic modeling of crystals, *JOM* 66 (2013) 399–407.
- [60] A. Stukowski, Visualization and analysis of atomistic simulation data with OVITO—the open visualization tool, *Modell. Simul. Mater. Sci. Eng.* 18 (2010) 015012.
- [61] P. Moazzen, M.R. Toroghinejad, T. Zargar, P. Cavaliere, Investigation of hardness, wear and magnetic properties of NiCoCrFeZrx HEA prepared through mechanical alloying and spark plasma sintering, *J. Alloys Compd.* 892 (2022) 161924.
- [62] J.R. Noonan, H.L. Davis, Truncation-induced multilayer relaxation of the Al(110) surface, *Phys. Rev. b* 29 (1984) 4349–4355.
- [63] R.W. Balluffi, Vacancy defect mobilities and binding energies obtained from annealing studies, *J. Nucl. Mater.* 69–70 (1978) 240–263.
- [64] C.B. Carter, I.L.F. Ray, On the stacking-fault energies of copper alloys, *Philos. Mag.* 35 (1977) 189–200.
- [65] S.F. Liu, Y. Wu, H.T. Wang, J.Y. He, J.B. Liu, C.X. Chen, X.J. Liu, H. Wang, Z.P. Lu, Stacking fault energy of face-centered-cubic high entropy alloys, *Intermetallics* 93 (2018) 269–273.
- [66] K.-T. Chen, T.-J. Wei, G.-C. Li, M.-Y. Chen, Y.-S. Chen, S.-W. Chang, H.-W. Yen, C.-S. Chen, Mechanical properties and deformation mechanisms in CoCrFeMnNi high entropy alloys: a molecular dynamics study, *Mater. Chem. Phys.* 271 (2021) 124912.
- [67] Z.J. Gu, Y.Z. Tian, W. Xu, S. Lu, X.L. Shang, J.W. Wang, G.W. Qin, Optimizing transformation-induced plasticity in CoCrNi alloys by combined grain refinement and chemical tuning, *Scr. Mater.* 214 (2022) 114658.
- [68] S.J. Sun, Y.Z. Tian, H.R. Lin, H.J. Yang, X.G. Dong, Y.H. Wang, Z.F. Zhang, Transition of twinning behavior in CoCrFeMnNi high entropy alloy with grain refinement, *Mater. Sci. Eng. a* 712 (2018) 603–607.
- [69] M.J. Sohrabi, H. Mirzadeh, S. Sadeghpour, R. Mahmudi, Grain size dependent mechanical behavior and TRIP effect in a metastable austenitic stainless steel, *Int. J. Plast.* 160 (2023) 103502.
- [70] X.H. An, S.D. Wu, Z.G. Wang, Z.F. Zhang, Significance of stacking fault energy in bulk nanostructured materials: insights from Cu and its binary alloys as model systems, *Prog. Mater Sci.* 101 (2019) 1–45.
- [71] P.H. Cao, The strongest size in gradient nanograined metals, *Nano Lett.* 20 (2020) 1440–1446.